Atmospheric
Chemistry
and Physics
Discussions

Open Access

1 **Aerosol pollution radiative effects on land carbon uptake in China**

2

3 Xu Yue[1] and Nadine Unger[2]

4

5 [1] Climate Change Research Center, Institute of Atmospheric Physics, Chinese Academy of

6 Sciences, Beijing 100029, China

7 [2] College of Engineering, Mathematics and Physical Sciences, University of Exeter, Exeter,

8 EX4 4QE, UK

9

10 *Correspondence to*: Xu Yue (yuexu@mail.iap.ac.cn)
11

12

Atmospheric
Chemistry
and Physics
Discussions

Open Access

13

14 **Abstract**

15

16 China suffers from frequent haze pollution episodes that alter the surface solar radiation and

17 influence regional carbon uptake by the land biosphere. Here, we apply combined vegetation

18 and radiation modeling and multiple observational datasets to assess the radiative effects of

19 aerosol pollution in China on the regional land carbon uptake for the 2009-2011 period. First,

20 we assess the inherent sensitivity of China's land biosphere to aerosol pollution by defining

21 and calculating two aerosol optical depth (AOD) at 550 nm thresholds (i) AOD_{t1}, resulting in

22 the maximum net primary productivity (NPP), and (ii) AOD_{t2}, such that if local AOD <

23 AOD_{t2}, the aerosol DFE always promotes local NPP compared with aerosol-free conditions.

24 Then, we apply the thresholds, satellite data, and interactive vegetation modeling to estimate

25 current impacts of aerosol pollution on land ecosystems. In the Northeast, observed AOD is

26 55% lower than AOD_{t1}, indicating strong aerosol DFE on local NPP. In the southeastern

27 coastal regions, observed AOD is close to AOD_{t1}, suggesting that regional NPP is promoted

28 by the current level of aerosol loading but that further increases in AOD in this region will

29 weaken the fertilization effects. The North China Plain experiences limited enhancement of

30 NPP by aerosols because observed AOD is 77% higher than AOD_{t1} but 14% lower than

31 AOD_{t2}. Aerosols always inhibit regional NPP in the Southwest because of the persistent high

32 cloud coverage that already substantially reduces the total light availability there. Under

33 clear-sky conditions, simulated NPP shows widespread increases of 20-60% (35.0 ± 0.9 % on

34 average) by aerosols. Under all-sky conditions, aerosol pollution has spatially contrasting

35 opposite sign effects on NPP from -3% to +6% (1.6 ± 0.5% on average), depending on the

36 local AOD relative to the regional thresholds. Stringent aerosol pollution reductions

37 motivated by public health concerns, especially in the North China Plain and the Southwest,

38 will help protect land ecosystem functioning in China and mitigate long-term global warming.

39

40

Atmospheric
Chemistry
and Physics
Discussions

Open Access

EGU

1 Introduction

Atmospheric aerosols scatter and absorb solar radiation, while plants rely on sunlight for photosynthesis. Thus, aerosols affect land carbon uptake through radiative perturbations. In particular, observations have demonstrated that aerosols can enhance canopy photosynthesis and light-use efficiency (LUE) by increasing diffuse radiation in the lower canopy (Gu et al., 2003; Rap et al., 2015; Strada et al., 2015). This aerosol diffuse fertilization effect (DFE) is subject to the aerosol loading and sky conditions (Cohan et al., 2002; Oliphant et al., 2011) because the potential benefit of increased diffuse radiation in the lower canopy can be offset or even reversed by the concomitant reductions in direct sunlight. China is the world largest anthropogenic emitter of carbon dioxide reaching 2.5 Pg C yr^{-1} (Liu et al., 2015), while the land ecosystems mitigate only around 0.2 Pg C yr^{-1} with large uncertainties (Piao et al., 2009). At the same time, China encounters frequent haze pollution events due to large emissions of anthropogenic aerosols and precursors (Guo et al., 2014; Wang and Chen, 2016). It is critically important to understand how this haze pollution affects the land carbon sink in China.

Leaf photosynthesis increases with the solar irradiance before reaching saturation (Farquhar et al., 1980). For a canopy with complex composition and vertical distribution, only sunlit leaves receive both direct and diffuse sunlight. Typically, irradiance is abundant for these leaves and photosynthesis is light saturated. In contrast, shaded leaves receive only diffuse radiation and their photosynthesis is usually light-limited (He et al., 2013). Existence of aerosol pollution and/or a cloud layer simultaneously increases diffuse radiation but decreases direct radiation. The enhancement of diffuse radiation helps increase photosynthesis by the shaded leaves but the response of the sunlit leaves depends on the level of aerosol/cloud loading. Moderate reductions of direct sunlight will not decrease photosynthesis of sunlit leaves because the light availability is still saturated. Consequently, the gross primary productivity (GPP) of the whole canopy (sunlit plus shaded portions) increases due to the improved LUE (Knohl and Baldocchi, 2008). Large reductions of direct sunlight may convert the light-saturated regime to light-limited regime for the sunlit leaves, leading to reduced LUE and dampened canopy GPP (Alton, 2008). Thus, the net effect of aerosol pollution on canopy carbon uptake depends on the aerosol loading, cloud amount, geographic location, and the plant species.

Previous observation-based studies of cloud and aerosol DFE are summarized in Table 1. Most observational studies have detected DFE using long-term ground-based measurements

Atmospheric
Chemistry
and Physics
Discussions

75   (Niyogi et al., 2004; Cirino et al., 2014). Currently, direct measurements of DFE on

76   photosynthesis in China are limited (Li et al., 2014). Observations suggest that both cloud

77   and aerosols exert similar impacts on land carbon uptake (Kanniah et al., 2012). Many

78   observational studies have found that canopy GPP of trees maximizes with diffuse fraction

79   (DF) of 0.4-0.7 (Rocha et al., 2004; Alton, 2008). For grass and savanna, the optimal DF is as

80   low as 0.2-0.3, above which the carbon uptake will decrease (Alton, 2008; Kanniah et al.,

81   2013). The appearance of thin cloud may enhance net ecosystem productivity (NEP) of trees

82   by 7-11% (Monson et al., 2002; Misson et al., 2005), while thick cloud reduces carbon

83   uptake due to large irradiance attenuation (Rocha et al., 2004). Aerosol light scattering in

84   clear sky may increase NEP of trees by 8-29% (Misson et al., 2005; Cirino et al., 2014), but

85   decreases the carbon uptake of grassland (Niyogi et al., 2004). Previous vegetation modeling

86   results are generally consistent with observations (Table 1). For example, Knohl and

87   Baldocchi (2008) predicted maximum GPP with DF of 0.45 for a deciduous forest.

88   In this study, we apply the **Y**ale **I**nteractive terrestrial **B**iosphere (YIBs) model (Yue and

89   Unger, 2015) combined with the **C**olumn **R**adiation **M**odel (CRM) to analyze the impacts of

90   aerosol DFE on net primary productivity (NPP) in China in the present day world. Our model

91   approach offers a large regional scale assessment (Mercado et al., 2009), and is not limited by

92   spatiotemporal and species-specific sampling issues (Table 1). We perform multiple

93   sensitivity experiments to derive the aerosol-induced DFE 'tolerance' of China's land

94   biosphere by defining and computing two thresholds of aerosol optical depth (AOD) at 550

95   nm: (i) AOD_{t1}, resulting in the maximum NPP, and (ii) AOD_{t2}, such that if local AOD <

96   AOD_{t2}, the aerosol DFE always promotes local NPP compared with aerosol-free conditions.

97   We consider aerosol-induced perturbations to diffuse, direct, and total photosynthetically

98   active radiation (PAR) under both clear and cloudy sky conditions, but ignore the

99   meteorological and hydrological feedbacks from those perturbations. Section 2 describes the

100   measurement data, vegetation and radiation models, and the full group of simulations.

101   Section 3 presents the model evaluation, the sensitivity of GPP to aerosol pollution in China,

102   the derived AOD thresholds, and the simulated NPP responses to current levels of aerosol

103   pollution. Section 4 summarizes and discusses the main results.

104

105

106   **2 Methods**

107

108   **2.1 The Yale Interactive Terrestrial Biosphere Model (YIBs)**

109 The YIBs is a process-based vegetation model that simulates global terrestrial carbon cycle
110 with dynamic predictions of leaf area index (LAI) and tree growth (Yue and Unger, 2015).
111 Plant photosynthesis is simulated using the well-established Farquhar scheme (Farquhar et al.,
112 1980) and is coupled to stomatal conductance with the Ball-Berry scheme (Ball et al., 1987).
113 The canopy radiative transfer scheme separates diffuse and direct PAR for sunlit and shaded
114 leaves (Spitters, 1986), depending on solar zenith angle and canopy LAI (section 2.3).
115 Autotrophic respiration (Ra) is split into maintenance and growth components, and is
116 dependent on leaf temperature and nitrogen content (Clark et al., 2011). The model includes 9
117 PFTs, including evergreen needleleaf forest (ENF), deciduous broadleaf forest (DBF),
118 evergreen broadleaf forest (EBF), shrubland, tundra, C3/C4 grassland, and C3/C4 cropland
119 (Fig. S1). This land cover is derived based on retrievals from both MODIS (Hansen et al.,
120 2003) and the Advanced Very High Resolution Radiometer (AVHRR) (Defries et al., 2000).
121 The fraction of C4 cropland is derived based on the total crop fraction and the ratio of C4
122 species (Monfreda et al., 2008).

123 The YIBs can be used in three different configurations: site-level, global/regional offline,
124 and online within a climate model. For this study, we use the regional offline version driven
125 with hourly 1°×1° meteorological forcings from the NASA Modern Era Retrospective-
126 analysis for Research and Applications (MERRA). On the global scale, simulated LAI, tree
127 height, phenology, GPP, and NPP show reasonable spatial distribution and long-term trends
128 compared with both *in situ* measurements and satellite retrievals (Yue and Unger, 2015; Yue
129 et al., 2015a; Yue et al., 2015b). Other carbon fluxes such as NEP, autotrophic respiration,
130 and heterotrophic respiration are also reasonably simulated relative to multiple model
131 ensembles (Yue et al., 2015b).

132

133 **2.2 The Column Radiation Model (CRM)**

134 The CRM is the standalone version of the radiation model used by the NCAR
135 Community Climate Model, which has been updated to the Community Earth System Model
136 (http://www.cesm.ucar.edu/models/). It calculates reflectivity and transmission of
137 atmospheric layers, emissivity and absorptivity of greenhouse gases (GHGs), and Mie
138 scattering and absorption of aerosols. Aerosol optical parameters associated with each aerosol
139 species, including specific extinction coefficients, single scattering albedo, and asymmetric
140 parameters, are adopted from Yue et al. (2010) for mineral dust, Yue and Liao (2012) for sea
141 salt, and RegCM4 model for other species (Giorgi et al., 2012). These parameters vary with
142 changes in both wavelength and relative humidity (Fig. S2). Sulfate and nitrate aerosols share

143   the same parameters. For carbonaceous aerosols (black carbon (BC) and organic carbon

144   (OC)), half are considered hydrophobic and half are hydrophilic.

145   The CRM is driven with hourly 1°×1° fields of temperature, humidity, and [O3] at 20

146   sigma levels interpolated from the MERRA data. Vertical profiles of cloud cover and liquid

147   water path are adopted from the CERES SYN1deg (http://ceres.larc.nasa.gov), which are

148   determined using remote sensing from MODIS and the Visible and Infrared Sounder (VIRS).

149   Surface albedo, temperature, and pressure are also adopted from MERRA. The model utilizes

150   aerosol profile of all species simulated by the ModelE2-YIBs, a fully coupled chemistry-

151   carbon-climate model (Schmidt et al., 2014). Aerosol components include sulfate, nitrate, BC,

152   OC, dust (clay and silt), and sea salt (accumulation and coarse modes). Concentrations of

153   these pollution species are predicted based on emission inventories of the year 2010 from the

154   Greenhouse Gas and Air Pollution Interactions and Synergies (GAINS) integrated assessment

155   model (Amann et al., 2011). We compare the GAINS v4a inventory with the HTAP

156   inventory adopted from the Emissions Database for Global Atmospheric Research (EDGAR,

157   http://edgar.jrc.ec.europa.eu) and RCP8.5 inventory from the Intergovernmental Panel on

158   Climate Change (IPCC, http://www.ipcc.ch/) (Fig. S3). The inter-comparison shows that the

159   GAINS has similar magnitude (differences within ±10%) of emissions for major pollutants

160   over China as HTAP and RCP8.5, except for ammonia, which is higher by 50-80% in

161   GAINS. Simulated summertime surface PM2.5 concentrations show high correlations

162   (R=0.76) and low biases (NMB=1.6%) with *in situ* measurements at 188 sites (not shown).

163

164   **2.3 Canopy radiative transfer and carbon uptake**

165   We use the multilayer canopy radiative transfer scheme proposed by Spitters (1986) to

166   separate diffuse and direct PAR for sunlit and shaded leaves. The canopy is divided into an

167   adaptive number of layers (typically 2-16) for light stratification. Light intensity decreases

168   exponentially with LAI when penetrating in the canopy:

169   $$I = (1 - \rho) \cdot I_t \cdot e^{-kL} \tag{1}$$

170   where I_t is the total PAR at the top of canopy, L is the LAI from the top of canopy to layer n,

171   I is the total PAR available for absorption at the depth L, and k is the extinction coefficient.

172   Here, ρ is the reflection coefficient calculated as follows:

173   $$\rho = \left(\frac{1 - (1 - \sigma)^{1/2}}{1 + (1 - \sigma)^{1/2}} \right) \left(\frac{2}{1 + 1.6 \cos \alpha} \right) \tag{2}$$

Atmospheric
Chemistry
and Physics
Discussions

174   where α is the solar zenith, $\sigma = 0.2$ is the scattering coefficient of single leaves. Light

175   absorption at the depth L is estimated as follows:

176    $$I_a = -dI/dL = (1 - \rho) \cdot I_t \cdot k \cdot e^{-kL} \qquad (3)$$

177   where I_a is the flux absorbed per unit leaf area. The total PAR at the top of canopy is consist

178   of diffuse (I_{tf}) and direct (I_{tr}) components, both of which are simulated with CRM model:

179    $$I_t = I_{tf} + I_{tr} \qquad (4)$$

180   According to equation (3), absorption of the diffuse flux is calculated as:

181    $$I_{fa} = (1 - \rho) \cdot I_{tf} \cdot k_f \cdot e^{-k_f L} \qquad (5)$$

182   where $k_f = 0.8(1-\sigma)^{1/2}$ is the extinction coefficient of the diffuse flux. For the direct flux, it is

183   segregated into diffuse and direct components on its way through the canopy. The total

184   absorption of direct flux is calculated as:

185    $$I_{ra} = (1 - \rho) \cdot I_{tr} \cdot (1 - \sigma)^{1/2} \cdot k_r \cdot e^{-(1-\sigma)^{1/2}k_r L} \qquad (6)$$

186   where $k_r = 0.5/\cos \alpha$ is the extinction coefficient of direct component of the direct flux. Here

187   the function $(1-\sigma)^{1/2}$ is applied to account for the scattering effects of leaves for direct light.

188   The absorption of the direct component of direct flux is calculated as:

189    $$I_{rra} = (1 - \sigma) \cdot I_{tr} \cdot k_r \cdot e^{-(1-\sigma)^{1/2}k_r L} \qquad (7)$$

190   We distinguish light absorption for shaded and sunlit leaves. Shaded leaves absorb diffuse

191   flux and the diffuse component of direct flux:

192    $$I_{sha} = I_{fa} + (I_{ra} - I_{rra}) \qquad (8)$$

193   Sunlit leaves absorb both diffuse and direct radiation:

194    $$I_{sla} = I_{sha} + (1 - \sigma) \cdot k_r \cdot I_{tr} \qquad (9)$$

195   Photosynthesis is calculated separately for shaded and sunlit leaves based on the different

196   light absorption. Canopy photosynthesis (μmol C s^{-1} per unit leaf area) is the sum of these

197   two parts of leaves:

198    $$A = f_{sl} \cdot A_{sl} + (1 - f_{sl}) \cdot A_{sh} \qquad (10)$$

199   where A_{sl} and A_{sh} are photosynthesis of sunlit and shaded leaves, respectively. The fraction of

200   sunlit leaf area f_{sl} is calculated as:

201    $$f_{sl} = e^{-k_r \cdot L} \qquad (11)$$

202   Finally, the total carbon uptake GPP (μmol C s^{-1} per unit ground area) is estimated as follows:

203    $$GPP = \int_0^{LAI} A \cdot dL \qquad (12)$$

204

Atmospheric
Chemistry
and Physics
Discussions

2.4 Simulations

We conduct simulations combining the offline YIBs vegetation model and the CRM radiation model. Diffuse and direct PAR at the top of canopy is predicted with CRM model. These radiative fluxes are then used as input for the YIBs model, which further separates diffuse and direct fluxes absorbed by sunlit and shaded leaves using Spitters (1986) canopy scheme. We perform two groups of YIBs-CRM sensitivity simulations, 30 for clear-sky conditions and 30 for all-sky conditions, to derive the AOD thresholds for aerosol DFE (Table 2). The YIBs model is driven with meteorological forcings from MERRA, except for direct and diffuse PAR, which is predicted with the CRM model. We set up baseline simulations (CLR010 and ALL010) with the aerosol profile from ModelE2-YIBs and validated optical parameters. In other simulations, specific scaling factors ranging from 0.0 to 30 are applied to aerosol concentrations to represent variations of AOD. Due to the disk storage limit for hourly meteorological profiles, we perform CRM simulations for 2009-2011. The simulated PAR is alternately applied as input for the YIBs model, which uses additional meteorological forcings from MERRA for 2000-2011. The last 3 years of YIBs output, including GPP and NPP, are used for analyses. We focus our analyses for the summer (June-July-August) season, when both AOD and carbon fluxes are high.

2.5 Benchmark and evaluation observational datasets

To evaluate GPP simulated with the YIBs model, we use global benchmark product upscaled from the FLUXNET eddy covariance data for 2009-2011 (Jung et al., 2009). For NPP, we use observations of 2009-2011 retrieved by the Moderate Resolution Imaging Spectroradiometer (MODIS) (Zhao et al., 2005). To evaluate surface radiative fluxes simulated with the CRM model, we use ground-based radiation data for 2008-2012 from 106 pyranometer sites in China, provided by the Climate Data Center, Chinese Meteorological Administration (Xia, 2010). For each site and each month, we derive the monthly mean radiative fluxes based on daily data if <30% days are missing. We then select sites that all months are available for 2008-2012, leaving a total of 95 sites for the evaluation of total shortwave radiation. Diffuse radiation is not observed at all sites, and only a total of 17 sites meet the criteria for the continuous measurements. For aerosol radiative effects, we use assimilation data of surface radiative fluxes adopted from the SYN1deg product of NASA Clouds and the Earth's Radiant Energy System (CERES) (Wielicki et al., 1996; Rutan et al., 2015). Aerosol effect in CERES is calculated with the Langley Fu-Liou radiative transfer model (Fu and Liou, 1993), using aerosol profiles simulated by the Model for Atmospheric

239   Transport and Chemistry (Rasch et al., 1997). We also use satellite-based AOD data from

240   MODIS (Remer et al., 2005) for model evaluations. All gridded data are interpolated onto

241   1°×1° grids, matching the resolution of both CRM and YIBs models.

242

243

244   **3 Results**

245

246   **3.1 Model evaluation**

247   The YIBs model predicts reasonable spatial distribution of carbon fluxes compared with

248   observations (Fig. 1). For the summer, high GPP and NPP is simulated in the Northeast,

249   Southwest, and southeastern coastal regions, where DBF and ENF trees dominate (Fig. S1).

250   The correlation coefficients between simulations and observations are as high as 0.8 for both

251   GPP and NPP. Predicted GPP is -24% lower on average than observed, mainly because the

252   model underestimates observations over North China Plain. The normalized mean bias (NMB)

253   of NPP is close to 0, because of the regional offsetting. On the annual mean basis,

254   simulations show higher correlations ($R = 0.84$ for GPP and 0.86 for NPP) and similar NMB

255   (-21% for GPP and -16% for NPP) compared with observations.

256   The CRM predicts opposite spatial distribution for total solar radiation and the

257   corresponding DF (Fig. 2). For radiation, high values are found in the North and West, while

258   low values in the East and Southwest. Such pattern is related to cloud cover, which is lower

259   in the north but higher in the south, especially the Southwest where cloud cover is usually

260   higher than 80% (Fig. S4). Due to the cloud scattering, those regions with low insolation

261   have high DF. Compared with *in situ* measurements, the simulated total radiation exhibits

262   reasonable spatial characteristics and the correlation coefficient is as high as 0.88. The

263   evaluation of DF shows certain biases but is reasonable over the East (blue points of Fig. 2f),

264   which is the major domain for this study.

265   The CRM also predicts reasonable AOD and aerosol radiative effects (Fig. 3). Using

266   aerosol concentrations from the climate model ModelE2-YIBs, the CRM simulates high

267   regional AOD centered in the North China Plain. Previous sensitivity tests with ModelE2-

268   YIBs shows that such high loading of aerosols is mainly (>80%) contributed by

269   anthropogenic emissions. The AOD is generally high over the vast domain of eastern China

270   but low in the western part. Compared with AOD from CERES, which is derived using

271   aerosol concentrations from a chemical transport model, the AOD in CRM presents

272   reasonable spatial distribution with high correlation coefficient of 0.7 and low NMB of -1%.

Atmospheric
Chemistry
and Physics
Discussions

273   However, compared with MODIS AOD, which is derived based on satellite retrievals, the

274   predicted AOD is on average overestimated by 30% in eastern China. For the following

275   analyses, we use the predicted AOD as the benchmark but discuss the influence of its

276   overestimation on the predicted aerosol DFE. We further assess aerosol radiative efficiency

277   (ARE), defined as radiative forcing per unit AOD, over China. Higher magnitude of ARE is

278   predicted in the North and West, because lower cloud coverage there allow larger radiative

279   perturbations by the same level of aerosols. The comparison of ARE between CRM and

280   CERES shows high correlation coefficient of 0.87. However, ARE in CRM is smaller by 21%

281   in magnitude than that in CERES.

282

283   **3.2 Sensitivity of GPP to DF and AOD in China**

284   Cloud and aerosols have similar scattering effects on solar radiation and DF. We

285   examine PFT-specific GPP responses to DF for clear and all-sky conditions (Fig. 4). Under

286   clear-sky conditions, at DF < 0.55, all PFTs show increased GPP in response to increasing

287   DF. Under these conditions, shaded leaves experience low light availability while

288   photosynthesis by sunlit leaves is light-saturated. Introduction of aerosol pollution to this

289   system redistributes sunlight to the shaded light-limited leaves (without compromising the

290   total light availability to sunlit leaves), thus increasing the LUE and GPP of the whole canopy.

291   The derived GPP-diffuse sensitivity (ΔGPP/ΔDF, units: g C m^{-2} day^{-1} per unit change of DF

292   with ± 95% confidence interval) is 5.4 ± 1.2 for ENF, 6.8 ± 2.1 for DBF, 5.6 ± 1.7 for shrub,

293   2.8 ± 0.7 for C3 herbs, and 2.2 ± 2.3 for C4 herbs when DF < 0.55. Although large variations

294   in GPP, denoted as error bars, exist within each bin, they do not affect the significance of the

295   GPP-diffuse responses. We select the GPP-diffuse sensitivity at clear-sky conditions

296   averaged for all PFTs as an example. The largest bin-to-bin difference in GPP is calculated as

297   1.9 g C m^{-2} day^{-1} between DF = 0.58 and DF = 0.12. Such GPP difference is significant at $p <$

298   0.001 level based on a Student T test, suggesting that GPP varies significantly when the DF

299   change is pronounced.

300   Under all-sky conditions, which includes both clear and cloudy skies, DF is always

301   higher than 0.55, because existing cloud cover has already increased the diffuse light fraction

302   in the system. Any further increase of DF by aerosol scattering has limited or even

303   detrimental impacts on whole canopy GPP because the associated aerosol-induced reductions

304   in direct radiation impact photosynthesis by the sunlit leaves. GPP decreases almost linearly

305   for all PFTs in response to increasing DF > 0.55, with GPP-diffuse sensitivity of -6.9 ± 1.4

306   for ENF, -10.8 ± 2.3 for DBF, -3.8 ± 1.7 for shrubland, -3.8 ± 0.8 for C3 herbs, and -10.1 ±

307   1.6 for C4 herbs. The GPP response to increases in DF > 0.55 is almost identical under clear-

308   sky and all-sky conditions.

309   The PFT-specific GPP responses to idealized perturbations in AOD depend strongly on

310   the sky conditions (Fig. 5). Under clear sky conditions, aerosol promotes GPP for most PFTs

311   if AOD < 2. The maximum possible enhancement of GPP is ~40% for DBF, ENF, and C3

312   herbs, and can be as high as 60% for shrub. Most shrub species (tundra plus arid shrub) are

313   located in the Southwest (Fig. S1). Over that region, solar irradiance is abundant at clear days

314   (not shown), allowing more efficient scattering for a given AOD. For a given AOD, the DFE

315   of C4 herbs is the weakest amongst PFTs with a maximum possible GPP enhancement of

316   only ~10%. C4 plants usually have lower LUE than C3 plants, and as a result more easily

317   become light-limited when aerosol attenuates total irradiance (Still et al., 2009; Kanniah et al.,

318   2012). A clear turning point is found for all species. For C3 plants, aerosol scattering

319   weakens GPP when AOD > 2, because photosynthesis of the sunlit leaves starts to become

320   light-limited due to reductions in direct insolation. For C4 plants, this turning point appears

321   earlier when AOD > 1. Under all-sky conditions, atmospheric aerosol shows neutral effects

322   on GPP when AOD < 1 and detrimental negative effects when AOD > 1 for all PFTs except

323   C4 (Fig. 4). For C4 plants, any addition of aerosol to the atmospheric column decreases GPP.

324   Our estimates of GPP sensitivity to DF and AOD are reasonable compared with previous

325   studies (Table 1) summarized as follows: (1) the maximum enhancement of GPP is 40% at

326   clear-sky conditions for most PFTs (Gu et al., 2003); (2) the GPP enhancement of C4 plants

327   is the least due to the lowest LUE compared with other PFTs (Still et al., 2009; Kanniah et al.,

328   2012); (3) the aerosol DFE is much stronger at clear-sky than that at all-sky conditions

329   (Cohan et al., 2002); (4) both cloud and aerosols exert similar DFE on land carbon uptake

330   (Kanniah et al., 2012; Cirino et al., 2014); and (5) the maximum GPP enhancement appears

331   when DF = 0.4-0.8 (Rocha et al., 2004; Alton, 2008; Zhang et al., 2010).

332

333   **3.3 Aerosol pollution DFE in China 2009-2011**

334   We apply the idealized GPP responses in Section 3.2 to estimate the current magnitude

335   of aerosol pollution DFE under realistic background conditions by defining 2 summertime

336   AOD thresholds across China (Fig. 6). The AOD thresholds are derived based on NPP (=

337   GPP – Ra), assuming no impacts of aerosol DFE on the autotrophic respiration Ra (Knohl

338   and Baldocchi, 2008). Now, we consider NPP responses, instead of GPP, because the former

339   represents the net carbon uptake by land ecosystems. The first threshold, AOD_{t1} is defined as

340   the AOD value with the maximum ΔNPP (the uppermost point of the response curve in Fig.

341   5), representing the saturation of DFE. The second threshold, AOD_{t2} is the cross point of the

342   response curve at zero ΔNPP. For each model grid cell, if AOD is close or equal to AOD_{t1},

343   the peak NPP is expected. If $AOD<AOD_{t2}$, aerosol DFE always promotes local NPP relative

344   to aerosol-free conditions (AOD=0).

345   We find relatively high AOD_{t1} in the Northeast and low values in the Southwest (23°-

346   35°N, 100°-105°E, box d in Fig. 6a), where average cloud cover is 80% in the summer (Fig.

347   S4). The pattern of AOD_{t2} is similar to that of AOD_{t1} (Fig. 6b), except for high values in the

348   North (42°-48°N, 105°-118°E), where insolation is high while average cloud fraction is less

349   than 50%. The values of the AOD thresholds are much higher for clear days; for example, the

350   average clear-sky AOD_{t1} is six times the all-sky values over the East (Fig. S5). Observed

351   summer AOD in the North China Plain (32°-40°N, 113°-120°E) exceeds AOD_{t1} by 77% but

352   is 14% lower than AOD_{t2} (Fig. 6c), suggesting limited aerosol DFE in this region. A

353   reduction of 44% in local AOD (so that AOD = AOD_{t1}) leads to the largest benefit for

354   regional carbon uptake. Both AOD_{t1} and AOD_{t2} in the Southwest are close to 0 (Fig. 6d),

355   indicating that appearance of aerosol always inhibits regional carbon uptake there. Observed

356   AOD in the Southeastern Coast (22°-°N, 110°-122°E) is approximately equal to AOD_{t1} (Fig.

357   6e) and that in the Northeast (40°-47°N, 122°-132°E) is 55% lower than AOD_{t1} (Fig. 6f),

358   indicating amplified carbon uptake by aerosol enhancements there.

359   To understand the relationship between the current AOD level and DFE, we calculate

360   differences between MODIS AOD and the thresholds (Fig. 7). The pattern is quite similar for

361   annual and summer differences, except that the former is less positive than the latter. The

362   stronger dampening effect by aerosols in summer is related to the higher seasonal AOD

363   (summer mean of 0.43 versus annual mean of 0.38) and cloud amount (summer mean of 65%

364   versus annual mean of 58%). Over the North China Plain and the Southwest, current AOD

365   level is larger than both AOD_{t1} and AOD_{t2}, suggesting that aerosols there on average inhibit

366   NPP and further increases in AOD lead to stronger inhibition. For southeastern coastal

367   regions, observed AOD is lower than AOD_{t2} but close to AOD_{t1} (Fig. 6e), suggesting that

368   aerosols there generally promote NPP relative to aerosol-free conditions. However, the

369   potential for stronger DFE is limited as further increases of AOD will dampen NPP. For the

370   North and Northeast, current AOD is far below AOD_{t1}, suggesting that appearance of

371   aerosols there boosts carbon uptake, and increases in AOD continue to increase NPP.

Atmospheric
Chemistry
and Physics
Discussions

372   We calculate perturbations in NPP for different sky conditions (Fig. 8), resulting from

373   the aerosol-induced perturbations in both direct and diffuse radiation (Fig. S6). Under clear

374   sky conditions, aerosol DFE causes widespread enhancement of NPP, ranging from 20% to

375   60% over the East and 1.14 ± 0.01 Pg C yr^{-1} (35.0 ± 0.9 %) for the whole China domain.

376   Under the all-sky conditions, aerosols drive weak patchy NPP responses, mainly because of

377   the high DF from existing cloud cover. Regional changes of NPP range from -3% to 6% and

378   the total change is 0.07 ± 0.02 Pg C yr^{-1} (1.6 ± 0.5%) over China.

379

380   **4 Discussion and conclusions**

381

382   We provide the first assessment of aerosol pollution radiative effects on land carbon uptake

383   in China today based on regional simulations that combine the CRM radiation model and the

384   YIBs vegetation model. The confidence level of our estimate is dependent on the capability

385   of these models to reproduce observed radiative and carbon fluxes, aerosol-induced radiative

386   perturbations, and GPP responses to these perturbations. For the first two aspects, we

387   evaluate CRM and YIBs models using *in situ*, satellite, and assimilation data (Figs. 1-3). The

388   simulated GPP-AOD relationship (Figs. 4-5) is reasonable compared with available

389   measurement and modeling results in the literature (Table 1).

390   Our estimate is subject to limitations and uncertainties. First, calculated aerosol DFE is

391   sensitive to the canopy radiative transfer scheme, We apply the widely used Spitters (1986)

392   scheme to separate diffuse and direct light for sunlit and shaded leaves (2-leaf mode). This

393   scheme invokes Beer's law that assumes light decays exponentially from the top to bottom of

394   canopy. The predicted maximum GPP enhancement of 40% is at the high end of the range of

395   previous modeling estimates (Table 1). A similar magnitude of GPP change was predicted by

396   Gu et al. (2003) using different parameterizations of light partitioning and leaf photosynthesis

397   (1-leaf mode). Mercado et al. (2009) predicted maximum GPP enhancement of only 18% for

398   deciduous trees, considering Beer's law for light extinction and a 2-leaf model for light

399   partitioning. Cohan et al. (2002) showed a maximum NPP enhancement of 17-30%

400   depending on the choice of canopy scheme. These discrepancies reveal large uncertainties

401   due to differences in the treatment of the canopy geometry (sphere or non-sphere), canopy

402   properties (e.g., leaf clumping factor, leaf inclination angle, and leaf optical properties), light

403   partitioning (diffuse or non-diffuse), and the upscaling of leaf photosynthesis (1-leaf or 2-

404 leaf). More observations are required to evaluate the different parameterizations and their use

405 in large-scale vegetation models.

406 Second, uncertainties in simulated AOD and aerosol radiative effects may affect the

407 derived aerosol DFE. For this study, simulated AOD is calculated based on the three

408 dimensional aerosol concentrations from ModelE2-YIBs climate model. Simulation shows

409 similar spatial pattern and magnitude compared with CERES product (Figs 3a-c), which also

410 uses aerosol profile from a chemical transport model. However, evaluations with MODIS

411 data show that the predicted AOD is on average overestimated by 30% in eastern China (not

412 shown). Considering that aerosol radiative efficiency from the CRM model is 21% lower

413 than that from Fu-Liou model (Figs 3d-f), our estimate of aerosol radiative perturbations in

414 China might be reasonable due to the offsetting biases in AOD and aerosol radiative

415 efficiency. On the other hand, even if we ignore the uncertainties from radiative transfer

416 scheme, the 30% overestimation in AOD does not cause large differences in the derived

417 aerosol DFE. As a check, we calculate ΔNPP in sensitivity experiments CLR007 and

418 ALL007 (Table 2), which employ AOD level lower by 30% than CLR010 and ALL010. We

419 find that clear-sky ΔNPP by aerosols is 0.91 Pg C yr^{-1} (27.7%) in CLR007, lower than the

420 enhancement of 35.0% in CLR010 (Fig. 8a). The all-sky ΔNPP by aerosols is 0.07 Pg C yr^{-1}

421 (1.6%) in ALL007, equal to the values derived from ALL010. The reason for such similarity

422 between ALL007 and ALL010 can be explained by the GPP-AOD relationship, which shows

423 that all-sky GPP is almost invariant when AOD<1 (Fig. 5). The results suggest that cloud

424 plays a dominant role in regulating diffuse radiation in China, and the aerosol DFE might be

425 secondary compared with cloud DFE.

426 Third, calculated aerosol DFE does not account for biotic feedbacks. Photosynthesis is

427 connected to plant physiological processes, such as stomatal conductance and respiration.

428 Observations have shown that aerosol DFE may increase water use efficiency (Rocha et al.,

429 2004; Knohl and Baldocchi, 2008), promoting plant growth and LAI that may further

430 increase canopy photosynthesis. We have assumed no responses in autotrophic respiration so

431 that the derived GPP-AOD relationship can be applied directly to NPP-AOD. Yet,

432 observations suggest that plant respiration decreases due to the aerosol-induced cooling

433 (Alton, 2008). Ignoring these biotic feedbacks indicates that NPP sensitivity to AOD

434 employed in our estimate may be underestimated.

435 Fourth, we omit the associated climatic responses to aerosol radiative effects. The

436 aerosol-induced radiative perturbations decrease surface temperature but increase relative

14

Atmospheric
Chemistry
and Physics
Discussions

437   humidity (because of decreased saturation water vapor pressure) (Jing et al., 2010; Cirino et

438   al., 2014). Increases in air humidity will help enhance plant water use efficiency, leading to

439   increased photosynthesis. The impact of cooling is uncertain depending on the relationship

440   between the local background temperature and the optimal temperature of photosynthesis,

441   which is about 25°C for most species (Farquhar et al., 1980). If leaf temperature is >25°C,

442   aerosol-induced cooling is beneficial for photosynthesis. On the contrary, if leaf temperature

443   is <25°C, the cooling will act to inhibit carbon uptake. Furthermore, cloud modification,

444   caused by both aerosol direct and indirect effects, may exert complex influences on land

445   ecosystems through perturbations in diffuse radiation, surface temperature, and precipitation.

446   Resolving these concomitant biotic, meteorological, and hydrological feedbacks requires

447   earth-system models that fully couple the land biosphere, atmospheric chemistry, radiation,

448   and climate.

449   Finally, the biogeochemical response to aerosol pollution-related reactive nitrogen (N)

450   deposition is not included. Simulations with the ModelE2-YIBs climate model show that

451   anthropogenic emissions contribute 90% of the total reactive inorganic and organic N

452   deposition in China, indicating potentially large impacts of anthropogenic aerosols on

453   regional carbon uptake through the coupled C-N cycle. Using a terrestrial ecosystem model,

454   Tian et al. (2011) proposed that anthropogenic N deposition and fertilizer applications

455   together account for 61 percent of the net carbon storage in China for the 1961-2005 period.

456   The carbon sequestered per gram of deposited nitrogen decreases gradually after the year

457   1985, suggesting that most areas have reached nitrogen saturation. Similarly, based on

458   satellite retrievals, Xiao et al. (2015) revealed that anthropogenic N deposition makes no

459   significant contributions to the increases of vegetation productivity during 1982-2006.

460   Therefore, additional fertilization from aerosol N deposition may be limited because many

461   areas have been N saturated for decades such that our estimate of ΔNPP due to aerosol effects

462   based on radiative changes (Fig. 8b) may be realistic.

463   Despite these uncertainties, our study reveals strong impacts of aerosol DFE on land

464   carbon uptake in China. Although aerosol DFE widely promotes NPP during clear days, NPP

465   shows strongly spatially contrasting responses under all-sky conditions. Aerosol pollution

466   increases NPP by 2-6% in the Northeast where both cloud coverage and particle loading is

467   moderate. Aerosol decreases NPP by 2-4% in both the North China Plain and the Southwest.

468   For the North China Plain, the NPP inhibition is related to the high local pollution level that

469   is above the AOD_{t2} threshold for carbon uptake. Our estimates show that a 44% reduction in

Atmospheric
Chemistry
and Physics
Discussions

Open Access

EGU

470 local aerosol AOD would help achieve the maximum benefits for plant productivity in this

471 region. In the Southwest, existing cloud cover is already dense and pollution aerosols inhibit

472 NPP in this region. Reductions of pollution aerosol loading will increase carbon uptake in

473 this region.

474

477

478

Atmospheric
Chemistry
and Physics
Discussions

Table 1. Summary of studies about diffuse fertilization effects (DFE).

Period	PFTs [a]	Lat.	Method	Diffusion metrics	Results [b]	Reference
1989-1990	DBF	42°S	Flux Obs.	Cloud	NEP is greater on cloudy days than clear days	Hollinger et al. (1994)
1997	Trees	> 53°N	Flux Obs.	Cloud	NEP is greater on cloudy days than clear days	Law et al. (2002)
1998-2000	ENF	40°N	Flux Obs.	Cloud	Maximum NEP is 11% higher on cloudy days than clear days	Monson et al. (2002)
1999-2001	DBF	46°N	Flux Obs.	Cloud	GPP is greater under partly cloudy than clear skies but is reduced under heavy cloud cover.	Rocha et al. (2004)
2002	ENF	39°N	Flux Obs.	Cloud	Mean NEP is 7% greater in cloudy than clear days	Misson et al. (2005)
1992-1993	DBF	43°N	Model	Cloud	Noontime GPP shows maximum increases of 40% by cloud	Gu et al. (2003)
1998-2002	Varied	36-71°N	Flux Obs.	AOD	NEP increases with aerosol loading for forest and crop, but decreases for grassland.	Niyogi et al. (2004)
2002	ENF	39°N	Flux Obs.	AOD	Afternoon NEP increases by 8% by aerosol	Misson et al. (2005)
1999-2002	EBF	10°S	Flux Obs.	AOD	NEP increases by 29% if AOD = 0.1-1.5	Cirino et al. (2014)
July 15th	ENF	30°N	Model	AOD	(1) NPP increase 30% at AOD = 0.6 for clear days (2) NPP decreases with AOD during cloudy days	Cohan et al. (2002)
1992-1993	DBF	43°N	Flux Obs.	Radiation	Noontime GPP increases by 23% by volcanic aerosols under clear sky	Gu et al. (2003)
1999-2003	Trees	3-61°N	Model	Radiation	GPP falls with decreased insolation	Alton et al. (2007)

Atmospheric
Chemistry
and Physics
Discussions

1999-2001	DBF	46°N	Flux Obs.	DF	Midday GPP is maximum at DF = 0.57	Rocha et al. (2004)
1992-1999	Varied	1°S-71°N	Flux Obs.	DF	GPP is maximum at DF = 0.4-0.7 for trees and shrubs, and DF = 0.2-0.3 for grass	Alton (2008)
2000-2002	DBF	51°N	Flux Obs.	DF	NEP is maximum at DF = 0.28-0.44	Moffat et al. (2010)
2001-2006	Savanna	12°S	Flux Obs.	DF	GPP decreases with increase of DF	Kanniah et al. (2013)
1999-2002	EBF	10°S	Flux Obs.	DF	NEP is maximum at DF = 0.6	Cirino et al. (2014)
2003-2013	Trees	36-46°N	Flux Obs.	DF	GPP is maximum at DF = 0.4-0.6	Strada et al. (2015)
2002	DBF	51°N	Model	DF	GPP is maximum at DF = 0.45	Knohl and Baldocchi (2008)
2002	DBF	51°N	Model	DF	Maximum GPP enhancement of 18% at DF = 0.4	Mercado et al. (2009)
2007	Herbs	36°N	Flux Obs.	CI [c]	NEP is maximum at CI = 0.37 (DF = 0.78)	Jing et al. (2010)
2003-2006	Trees	23-36°N	Flux Obs.	CI	NEP is maximum at CI = 0.4-0.6 (DF = 0.36-0.73)	Zhang et al. (2010)
2008-2009	Herbs	38°N	Flux Obs.	CI	NEP is maximum at CI = 0.4-0.7 (DF = 0.18-0.73)	Bai et al. (2012)

[a] Plant functional types (PFTs) include evergreen needleleaf forest (ENF), deciduous broadleaf forest (DBF), evergreen broadleaf forest (EBF), trees (mixture of ENF/DBF/EBF and shrub), herbs (grass and crop), and savanna.
[b] Carbon metrics include gross primary productivity (GPP), net primary productivity (NPP), and net ecosystem productivity (NEP).
[c] Clearness index (CI) is converted to diffuse fraction (DF) with DF = 1.45 − 1.81×CI (Alton, 2008).

Atmospheric
Chemistry
and Physics
Discussions

Open Access

EGU

Table 2. Summary of 60 YIBs-CRM simulations.

Simulations	AOD ratio [a]	Sky condition	Simulations	AOD ratio	Sky condition
CLR000	0.0	Clear sky [b]	ALL000	0.0	All sky [c]
CLR001	0.1	Clear sky	ALL001	0.1	All sky
CLR002	0.2	Clear sky	ALL002	0.2	All sky
CLR003	0.3	Clear sky	ALL003	0.3	All sky
CLR004	0.4	Clear sky	ALL004	0.4	All sky
CLR005	0.5	Clear sky	ALL005	0.5	All sky
CLR006	0.6	Clear sky	ALL006	0.6	All sky
CLR007	0.7	Clear sky	ALL007	0.7	All sky
CLR008	0.8	Clear sky	ALL008	0.8	All sky
CLR009	0.9	Clear sky	ALL009	0.9	All sky
CLR010	1.0	Clear sky	ALL010	1.0	All sky
CLR012	1.2	Clear sky	ALL012	1.2	All sky
CLR014	1.4	Clear sky	ALL014	1.4	All sky
CLR016	1.6	Clear sky	ALL016	1.6	All sky
CLR018	1.8	Clear sky	ALL018	1.8	All sky
CLR020	2.0	Clear sky	ALL020	2.0	All sky
CLR025	2.5	Clear sky	ALL025	2.5	All sky
CLR030	3.0	Clear sky	ALL030	3.0	All sky
CLR035	3.5	Clear sky	ALL035	3.5	All sky
CLR040	4.0	Clear sky	ALL040	4.0	All sky
CLR050	5.0	Clear sky	ALL050	5.0	All sky
CLR060	6.0	Clear sky	ALL060	6.0	All sky
CLR070	7.0	Clear sky	ALL070	7.0	All sky
CLR080	8.0	Clear sky	ALL080	8.0	All sky
CLR100	10.0	Clear sky	ALL100	10.0	All sky
CLR120	12.0	Clear sky	ALL120	12.0	All sky
CLR150	15.0	Clear sky	ALL150	15.0	All sky
CLR200	20.0	Clear sky	ALL200	20.0	All sky
CLR250	25.0	Clear sky	ALL250	25.0	All sky
CLR300	30.0	Clear sky	ALL300	30.0	All sky

[a] We amplify or diminish base AOD by a certain ratio for each simulation. The base AOD (Fig. 3a) is derived with the aerosol profiles from ModelE2-YIBs climate model and optical parameters from multiple data sources (Fig. S2).
[b] For clear-sky simulations, cloud cover and liquid water path are set to zero.
[c] For all-sky simulations, cloud cover and liquid water path are adopted from the Clouds and the Earth's Radiant Energy System (CERES) SYN1deg Product.

Reference

Alton, P. B., North, P. R., and Los, S. O.: The impact of diffuse sunlight on canopy light-use efficiency, gross photosynthetic product and net ecosystem exchange in three forest biomes, Global Change Biol, 13, 776-787, doi:10.1111/j.1365-2486.2007.01316.x, 2007.

Alton, P. B.: Reduced carbon sequestration in terrestrial ecosystems under overcast skies compared to clear skies, Agr Forest Meteorol, 148, 1641–1653, doi:10.1016/j.agrformet.2008.05.014, 2008.

Amann, M., Bertok, I., Borken-Kleefeld, J., Cofala, J., Heyes, C., Hoglund-Isaksson, L., Klimont, Z., Nguyen, B., Posch, M., Rafaj, P., Sandler, R., Schopp, W., Wagner, F., and Winiwarter, W.: Cost-effective control of air quality and greenhouse gases in Europe: Modeling and policy applications, Environ Modell Softw, 26, 1489-1501, doi:10.1016/j.envsoft.2011.07.012, 2011.

Bai, Y., Wang, J., Zhang, B., Zhang, Z., and Liang, J.: Comparing the impact of cloudiness on carbon dioxide exchange in a grassland and a maize cropland in northwestern China, Ecol Res, 27, 615-623, doi:10.1007/s11284-012-0930-z, 2012.

Ball, J. T., Woodrow, I. E., and Berry, J. A.: A model predicting stomatal conductance and its contribution to the control of photosyn- thesis under different environmental conditions, in: Progress in Photosynthesis Research, edited by: Biggins, J., Nijhoff, Dordrecht, Netherlands, 110–112, 1987.

Cirino, G. G., Souza, R. A. F., Adams, D. K., and Artaxo, P.: The effect of atmospheric aerosol particles and clouds on net ecosystem exchange in the Amazon, Atmos Chem Phys, 14, 6523-6543, doi:10.5194/acp-14-6523-2014, 2014.

Clark, D. B., Mercado, L. M., Sitch, S., Jones, C. D., Gedney, N., Best, M. J., Pryor, M., Rooney, G. G., Essery, R. L. H., Blyth, E., Boucher, O., Harding, R. J., Huntingford, C., and Cox, P. M.: The Joint UK Land Environment Simulator (JULES), model description - Part 2: Carbon fluxes and vegetation dynamics, Geosci Model Dev, 4, 701-722, doi:10.5194/Gmd-4-701-2011, 2011.

Cohan, D. S., Xu, J., Greenwald, R., Bergin, M. H., and Chameides, W. L.: Impact of atmospheric aerosol light scattering and absorption on terrestrial net primary productivity, Global Biogeochem Cy, 16, 1090, doi:10.1029/2001gb001441, 2002.

Defries, R. S., Hansen, M. C., Townshend, J. R. G., Janetos, A. C., and Loveland, T. R.: A new global 1-km dataset of percentage tree cover derived from remote sensing, Global Change Biol, 6, 247-254, doi:10.1046/J.1365-2486.2000.00296.X, 2000.

Farquhar, G. D., Caemmerer, S. V., and Berry, J. A.: A Biochemical-Model of Photosynthetic Co2 Assimilation in Leaves of C-3 Species, Planta, 149, 78-90, doi:10.1007/Bf00386231, 1980.

Fu, Q., and Liou, K. N.: Parameterization of the Radiative Properties of Cirrus Clouds, Journal of Atmospheric Sciences, 50, 2008-2025, 1993.

Giorgi, F., Coppola, E., Solmon, F., Mariotti, L., Sylla, M. B., Bi, X., Elguindi, N., Diro, G. T., Nair, V., Giuliani, G., Turuncoglu, U. U., Cozzini, S., Guttler, I., O'Brien, T. A., Tawfik, A. B., Shalaby, A., Zakey, A. S., Steiner, A. L., Stordal, F., Sloan, L. C., and Brankovic, C.: RegCM4: model description and preliminary tests over multiple CORDEX domains, Clim. Res., 52, 7-29, doi:10.3354/cr01018, 2012.

Gu, L. H., Baldocchi, D. D., Wofsy, S. C., Munger, J. W., Michalsky, J. J., Urbanski, S. P., and Boden, T. A.: Response of a deciduous forest to the Mount Pinatubo eruption: Enhanced photosynthesis, Science, 299, 2035-2038, doi:10.1126/science.1078366, 2003.

Guo, S., Hu, M., Zamora, M. L., Peng, J., Shang, D., Zheng, J., Du, Z., Wu, Z., Shao, M., Zeng, L., Molina, M. J., and Zhang, R.: Elucidating severe urban haze formation in China, P Natl Acad Sci USA, 111, 17373-17378, 2014.

Hansen, M. C., DeFries, R. S., Townshend, J. R. G., Carroll, M., Dimiceli, C., and Sohlberg, R. A.: Global Percent Tree Cover at a Spatial Resolution of 500 Meters: First Results of the MODIS Vegetation Continuous Fields Algorithm, Earth Interact, 7, 1-15, doi:10.1175/1087-3562(2003)007<0001:GPTCAA>2.0.CO;2, 2003.

He, M. Z., Ju, W. M., Zhou, Y. L., Chen, J. M., He, H. L., Wang, S. Q., Wang, H. M., Guan, D. X., Yan, J. H., Li, Y. N., Hao, Y. B., and Zhao, F. H.: Development of a two-leaf light use efficiency model for improving the calculation of terrestrial gross primary productivity, Agr Forest Meteorol, 173, 28-39, doi:Doi 10.1016/J.Agrformet.2013.01.003, 2013.

Hollinger, D. Y., Kelliher, F. M., Byers, J. N., and Hunt, J. E.: Carbon dioxide exchange between an undisturbed old-growth temperate forest and the atmosphere, Ecology, 75, 134-150, 1994.

Jing, X., Huang, J., Wang, G., Higuchi, K., Bi, J., Sun, Y., Yu, H., and Wang, T.: The effects of clouds and aerosols on net ecosystem CO_2 exchange over semi-arid Loess Plateau of Northwest China, Atmos Chem Phys, 10, 8205-8218, doi:10.5194/acp-10-8205-2010, 2010.

Jung, M., Reichstein, M., and Bondeau, A.: Towards global empirical upscaling of FLUXNET eddy covariance observations: validation of a model tree ensemble approach using a biosphere model, Biogeosciences, 6, 2001-2013, doi:10.5194/bg-6-2001-2009, 2009.

Kanniah, K. D., Beringer, J., North, P., and Hutley, L.: Control of atmospheric particles on diffuse radiation and terrestrial plant productivity: A review, Prog Phys Geog, 36, 209-237, doi:10.1177/0309133311434244, 2012.

Kanniah, K. D., Beringer, J., and Hutley, L.: Exploring the link between clouds, radiation, and canopy productivity of tropical savannas, Agr Forest Meteorol, 182-183, 304-313, doi:10.1016/j.agrformet.2013.06.010, 2013.

Knohl, A., and Baldocchi, D. D.: Effects of diffuse radiation on canopy gas exchange processes in a forest ecosystem, J Geophys Res-Biogeo, 113, G02023, doi:10.1029/2007JG000663, 2008.

Law, B. E., Falge, E., Gu, L., Baldocchi, D. D., Bakwin, P., Berbigier, P., Davis, K., Dolman, A. J., Falk, M., Fuentes, J. D., Goldstein, A., Granier, A., Grelle, A., Hollinger, D., Janssens, I. A., Jarvis, P., Jensen, N. O., Katul, G., Mahli, Y., Matteucci, G., Meyers, T., Monson, R., Munger, W., Oechel, W., Olson, R., Pilegaard, K., Paw, K. T., Thorgeirsson, H., Valentini, R., Verma, S., Vesala, T., Wilson, K., and Wofsy, S.: Environmental controls over carbon dioxide and water vapor exchange of terrestrial vegetation, Agr Forest Meteorol, 113, 97-120, doi:10.1016/S0168-1923(02)00104-1, 2002.

Li, T., Heuvelink, E., Dueck, T. A., Janse, J., Gort, G., and Marcelis, L. F. M.: Enhancement of crop photosynthesis by diffuse light: quantifying the contributing factors, Annales of Botany, 114, 145-156, 2014.

Liu, Z., Guan, D. B., Wei, W., Davis, S. J., Ciais, P., Bai, J., Peng, S. S., Zhang, Q., Hubacek, K., Marland, G., Andres, R. J., Crawford-Brown, D., Lin, J. T., Zhao, H. Y., Hong, C. P., Boden, T. A., Feng, K. S., Peters, G. P., Xi, F. M., Liu, J. G., Li, Y., Zhao, Y., Zeng, N., and He, K. B.: Reduced carbon emission estimates from fossil fuel combustion and cement production in China, Nature, 524, 335-338, doi:10.1038/nature14677, 2015.

Mercado, L. M., Bellouin, N., Sitch, S., Boucher, O., Huntingford, C., Wild, M., and Cox, P. M.: Impact of changes in diffuse radiation on the global land carbon sink, Nature, 458, 1014-U1087, doi:10.1038/Nature07949, 2009.

Misson, L., Lunden, M., McKay, M., and Goldsteina, A. H.: Atmospheric aerosol light scattering and surface wetness influence the diurnal pattern of net ecosystem exchange in a semi-arid ponderosa pine plantation, Agr Forest Meteorol, 129, 69-83, 2005.

Moffat, A. M., Beckstein, C., Churkina, G., Mund, M., and Heimann, M.: Characterization of ecosystem responses to climatic controls using artificial neural networks, Global Change Biol, 16, 2737-2749, doi:10.1111/J.1365-2486.2010.02171.X, 2010.

Monfreda, C., Ramankutty, N., and Foley, J. A.: Farming the planet: 2. Geographic distribution of crop areas, yields, physiological types, and net primary production in the year 2000, Global Biogeochem Cy, 22, Gb1022, doi:10.1029/2007gb002947, 2008.

Monson, R. K., Turnipseed, A. A., Sparks, J. P., Harley, P. C., Scott-Denton, L. E., Sparks, K., and uxman, T. E.: Carbon sequestration in a high-elevation, subalpine forest, Global Change Biol, 8, 459-478, doi:10.1046/j.1365-2486.2002.00480.x, 2002.

Niyogi, D., Chang, H.-I., Saxena, V. K., Holt, T., Alapaty, K., Booker, F., Chen, F., Davis, K. J., Holben, B., Matsui, T., Meyers, T., Oechel, W. C., Sr., R. A. P., Wells, R., Wilson, K., and Xue, Y.: Direct observations of the effects of aerosol loading on net ecosystem CO_2 exchanges over different landscapes, Geophys Res Lett, 31, doi:10.1029/2004GL020915, 2004.

Oliphant, A. J., Dragoni, D., Deng, B., Grimmond, C. S. B., Schmid, H. P., and Scott, S. L.: The role of sky conditions on gross primary production in a mixed deciduous forest, Agr Forest Meteorol, 151, 781-791, doi:10.1016/J.Agrformet.2011.01.005, 2011.

Piao, S. L., Fang, J. Y., Ciais, P., Peylin, P., Huang, Y., Sitch, S., and Wang, T.: The carbon balance of terrestrial ecosystems in China, Nature, 458, 1009-1013, doi:10.1038/nature07944, 2009.

Rap, A., Spracklen, D. V., Mercado, L., Reddington, C. L., Haywood, J. M., Ellis, R. J., Phillips, O. L., Artaxo, P., Bonal, D., Coupe, N. R., and Butt, N.: Fires increase Amazon forest productivity through increases in diffuse radiation, Geophys Res Lett, 42, 4654-4662, doi:10.1002/2015gl063719, 2015.

Rasch, P. J., Mahowald, N. M., and Eaton, B. E.: Representations of transport, convection, and the hydrologic cycle in chemical transport models: Implications for the modeling of short-lived and soluble species, J Geophys Res-Biogeo, 102, 28127–28138, doi:10.1029/97JD02087, 1997.

Remer, L. A., Kaufman, Y. J., Tanré, D., Mattoo, S., Chu, D. A., Martins, J. V., Li, R.-R., Ichoku, C., Levy, R. C., Kleidman, R. G., Eck, T. F., Vermote, E., and Holben, B. N.: The MODIS Aerosol Algorithm, Products, and Validation, Journal of Atmospheric Sciences, 62, 947-973, 2005.

Rocha, A. V., Su, H. B., Vogel, C. S., Schmid, H. P., and Curtis, P. S.: Photosynthetic and water use efficiency responses to diffuse radiation by an aspen-dominated northern hardwood forest, Forest Sci, 50, 793-801, 2004.

Rutan, D. A., Kato, S., Doelling, D. R., Rose, F. G., Nguyen, L. T., Caldwell, T. E., and Loeb, N. G.: CERES Synoptic Product: Methodology and Validation of Surface Radiant Flux, Journal of Atmospheric and Oceanic Technology, 32, 1121-1143, doi:10.1175/JTECH-D-14-00165.1, 2015.

Schmidt, G. A., Kelley, M., Nazarenko, L., Ruedy, R., Russell, G. L., Aleinov, I., Bauer, M., Bauer, S. E., Bhat, M. K., Bleck, R., Canuto, V., Chen, Y. H., Cheng, Y., Clune, T. L., Del Genio, A., de Fainchtein, R., Faluvegi, G., Hansen, J. E., Healy, R. J., Kiang, N. Y., Koch, D., Lacis, A. A., LeGrande, A. N., Lerner, J., Lo, K. K., Matthews, E. E., Menon, S., Miller, R. L., Oinas, V., Oloso, A. O., Perlwitz, J. P., Puma, M. J., Putman, W. M., Rind, D., Romanou, A., Sato, M., Shindell, D. T., Sun, S., Syed, R. A., Tausnev, N., Tsigaridis, K., Unger, N., Voulgarakis, A., Yao, M. S., and Zhang, J. L.: Configuration and assessment of the GISS ModelE2 contributions to the CMIP5 archive, J Adv Model Earth Sy, 6, 141-184, doi:10.1002/2013ms000265, 2014.

Spitters, C. J. T.: Separating the Diffuse and Direct Component of Global Radiation and Its Implications for Modeling Canopy Photosynthesis .2. Calculation of Canopy

Photosynthesis, Agr Forest Meteorol, 38, 231-242, doi:10.1016/0168-1923(86)90061-4, 1986.

Still, C. J., Riley, W. J., Biraud, S. C., Noone, D. C., Buenning, N. H., Randerson, J. T., Torn, M. S., Welker, J., White, J. W. C., Vachon, R., Farquhar, G. D., and Berry, J. A.: Influence of clouds and diffuse radiation on ecosystem-atmosphere CO_2 and (COO)-O-18 exchanges, J. Geophys. Res., 114, G01018, doi:10.1029/2007jg000675, 2009.

Strada, S., Unger, N., and Yue, X.: Observed aerosol-induced radiative effect on plant productivity in the eastern United States, Atmos. Environ., 122, 463–476, doi:10.1016/j.atmosenv.2015.09.051, 2015.

Tian, H. Q., Melillo, J., Lu, C. Q., Kicklighter, D., Liu, M. L., Ren, W., Xu, X. F., Chen, G. S., Zhang, C., Pan, S. F., Liu, J. Y., and Running, S.: China's terrestrial carbon balance: Contributions from multiple global change factors, Global Biogeochem Cy, 25, Gb1007, doi:10.1029/2010gb003838, 2011.

Wang, H. J., and Chen, H. P.: Understanding the recent trend of haze pollution in eastern China: roles of climate change, Atmos. Chem. Phys., 16, 4205-4211, doi:10.5194/acp-16-4205-2016, 2016.

Wielicki, B. A., Barkstrom, B. R., Harrison, E. F., Lee, R. B., Smith, G. L., and Cooper, J. E.: Clouds and the earth's radiant energy system (CERES): An earth observing system experiment, B Am Meteorol Soc, 77, 853-868, doi:10.1175/1520-0477(1996)077<0853:Catere>2.0.Co;2, 1996.

Xia, X.: A closer looking at dimming and brightening in China during 1961-2005, Ann Geophys-Germany, 28, 1121-1132, doi:10.5194/angeo-28-1121-2010, 2010.

Xiao, J. F., Zhou, Y., and Zhang, L.: Contributions of natural and human factors to increases in vegetation productivity in China, Ecosphere, 6, 233, doi:10.1890/Es14-00394.1, 2015.

Yue, X., Wang, H., Liao, H., and Fan, K.: Simulation of dust aerosol radiative feedback using the GMOD: 2. Dust-climate interactions, J. Geophys. Res., 115, D04201, doi:10.1029/2009JD012063, 2010.

Yue, X., and Liao, H.: Climatic responses to the shortwave and longwave direct radiative effects of sea salt aerosol in present day and the last glacial maximum, Clim. Dyn., 39, 3019-3040, doi:10.1007/S00382-012-1312-5, 2012.

Yue, X., and Unger, N.: The Yale Interactive terrestrial Biosphere model version 1.0: description, evaluation and implementation into NASA GISS ModelE2, Geosci. Model Dev., 8, 2399-2417, doi:10.5194/gmd-8-2399-2015, 2015.

Yue, X., Unger, N., Keenan, T. F., Zhang, X., and Vogel, C. S.: Probing the past 30-year phenology trend of U.S. deciduous forests, Biogeosciences, 12, 4693-4709, doi:10.5194/bg-12-4693-2015, 2015a.

Yue, X., Unger, N., and Zheng, Y.: Distinguishing the drivers of trends in land carbon fluxes and biogenic emissions over the past three decades, Atmos. Chem. Phys. , 15, 11931-11948, doi:10.5194/acp-15-11931-2015, 2015b.

Zhang, M., Yu, G. R., Zhang, L. M., Sun, X. M., Wen, X. F., Han, S. J., and Yan, J. H.: Impact of cloudiness on net ecosystem exchange of carbon dioxide in different types of forest ecosystems in China., Biogeosciences, 7, 711-722, doi:10.5194/bg-7-711-2010, 2010.

Zhao, M. S., Heinsch, F. A., Nemani, R. R., and Running, S. W.: Improvements of the MODIS terrestrial gross and net primary production global data set, Remote Sens Environ, 95, 164-176, doi:10.1016/J.Rse.2004.12.011, 2005.
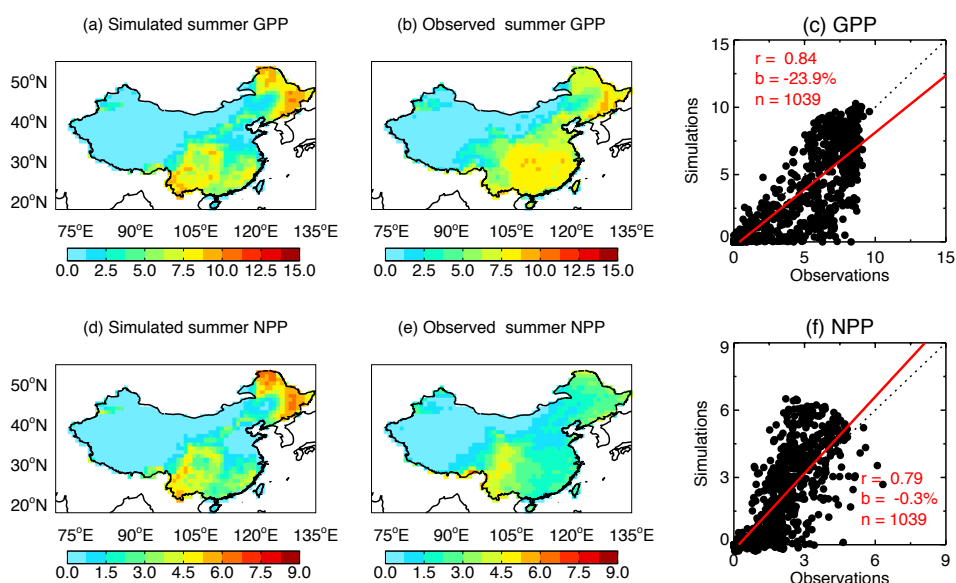
Atmospheric
Chemistry
and Physics
Discussions

Open Access

EGU

Figure 1. Evaluation of summertime carbon fluxes simulated with the YIBs model. Simulations are (a) GPP and (d) NPP from ALL010. Observations of carbon fluxes are averaged for 2009-2011, with (b) GPP from the upscaling of flux tower data and (e) NPP from the Moderate Resolution Imaging Spectroradiometer (MODIS). The aerosol DFE is included in the simulation. The correlation coefficients (r), relative biases (b), and number of $1° \times 1°$ grid cells (n) for the comparisons are listed on the scatter plots (c and f). Units: g C m^{-2} day^{-1}.
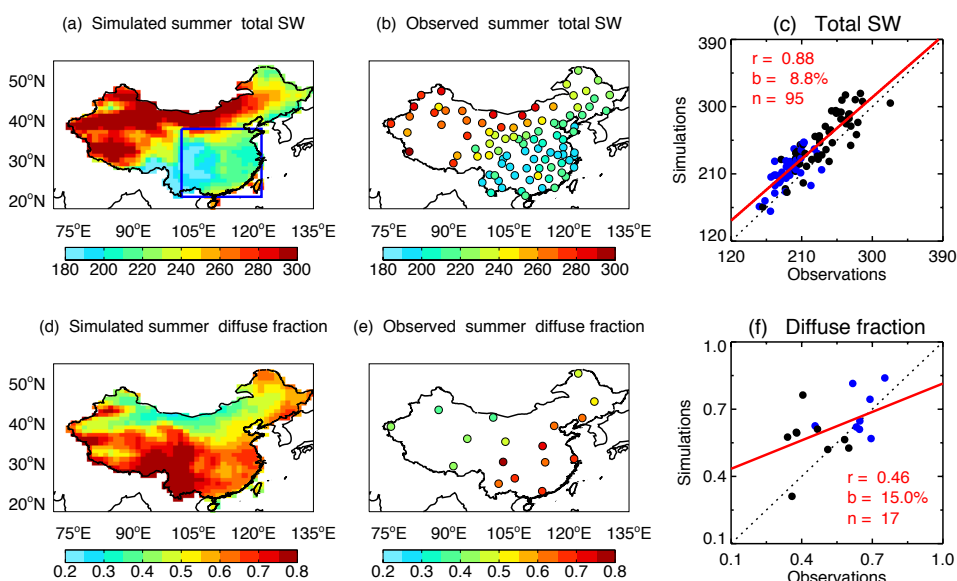
Figure 2. Evaluation of summertime radiation fluxes simulated with the CRM model. Simulations are (a) surface total shortwave radiation (W m^{-2}) and (d) diffuse radiation fraction from ALL010 with 1°×1° resolution. Observations (b and e) are the average during 2008-2012 from 106 sites operated by the Climate Data Center, Chinese Meteorological Administration. The correlation coefficients (r), relative biases (b), and number of sites (n) are shown in the scatter plots (c and f). The blue points in the scatter plots represent sites located within the box regions in eastern China as shown in (a).
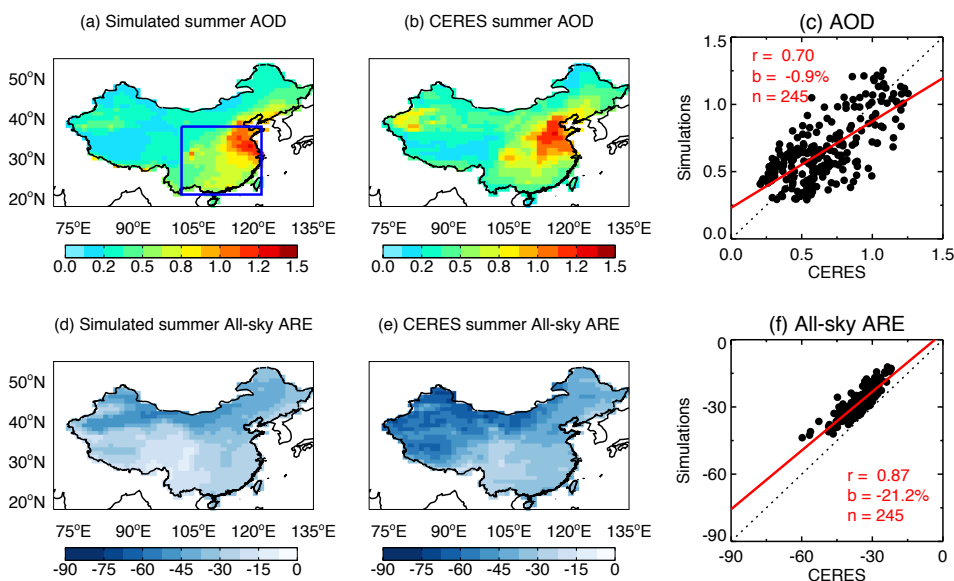
Figure 3. Evaluation of aerosol radiative effects simulated with the CRM model. Panels show the simulated (a) AOD at 550 nm and (d) all-sky aerosol radiative efficiency (ARE, W m^{-2} per unit AOD) with that from the CERES SYN1deg Product (b, e). The correlation coefficients (r), relative biases (b), and number of 1°×1° grid cells (n) for the comparisons over the box domain in figure (a) are listed on the scatter plots (c, f).
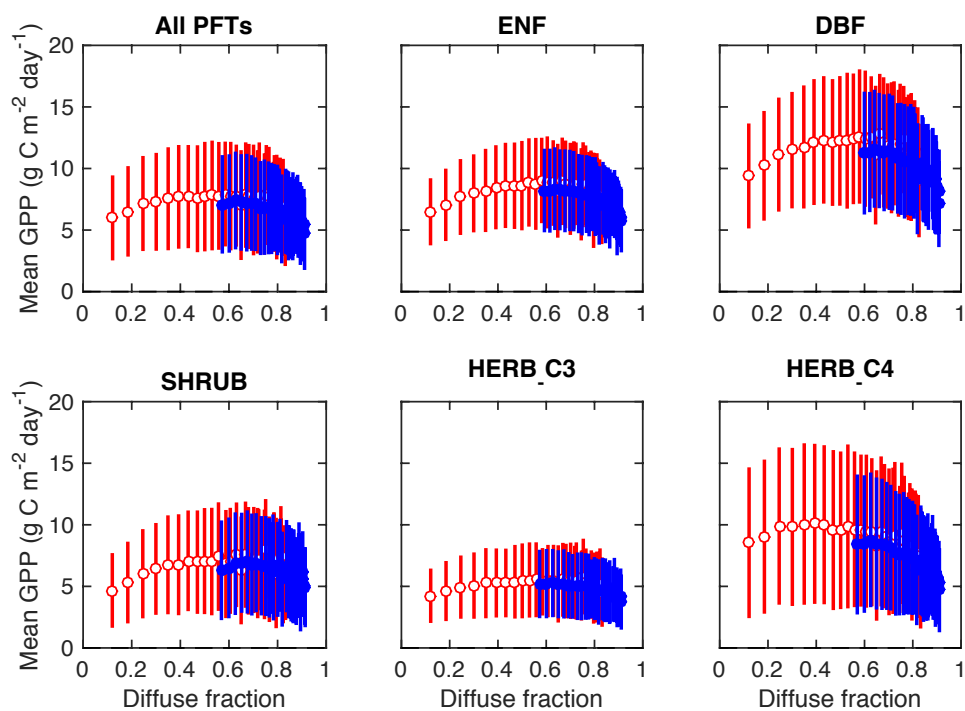
Figure 4. Mean summer GPP for different diffuse fractions. Results shown are for clear-sky (red empty points) and all-sky (blue solid points) conditions. Separately for clear-sky and all-sky conditions, we first collect all grid cells in eastern China (box region in Fig. 2a) for all 30 sensitivity simulations. We then aggregate all grid cells with non-zero fraction of a specific PFT into 30 AOD bins ranging from 0 to 6 at an interval of 0.2. In each bin, we calculate average diffuse fraction and corresponding GPP, with an error bar indicating one standard deviation.
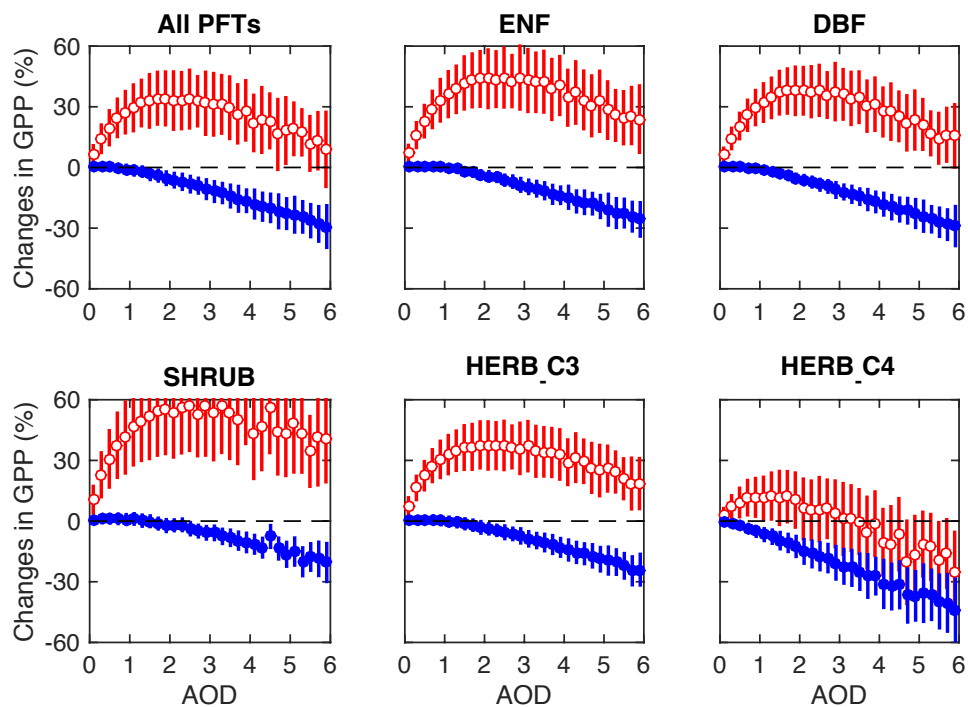
Figure 5. Sensitivity of summer GPP to changes of AOD. Results shown are different for clear-sky (red empty points) and all-sky (blue solid points) conditions in summer (June-August). Separately for clear-sky and all-sky conditions, we first collect all grid cells in eastern China (box region in Fig. 2a) for all 30 sensitivity simulations (Table 2). We then aggregate all grid cells with non-zero fraction of the specific PFT into 30 AOD bins ranging from 0 to 6 at an interval of 0.2. In each bin, we calculate average GPP change relative to aerosol-free conditions, with an error bar indicating one standard deviation.
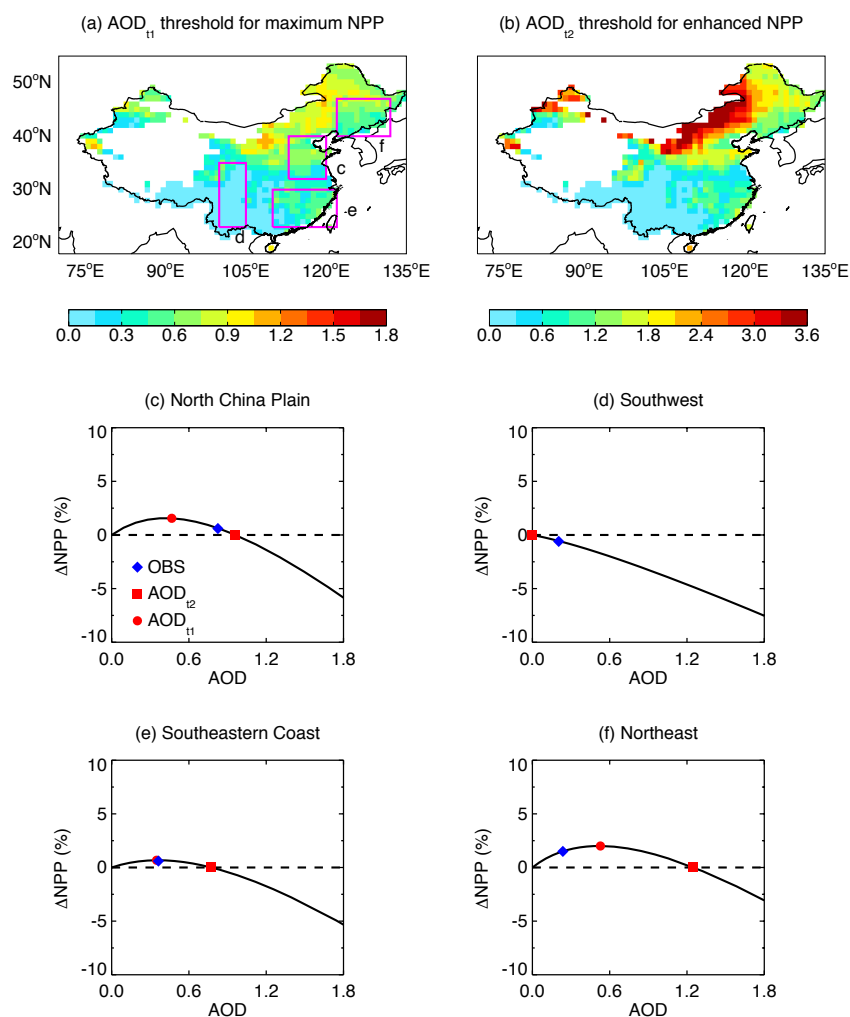
Figure 6. Thresholds of AOD at 550 nm for aerosol DFE. (a) AOD_{t1} threshold leading to maximum NPP in summer (June-August). (b) AOD_{t2} threshold leading to enhanced summer NPP. Aerosol indirect effects and climatic feedback are not included for these thresholds. The average AOD-NPP response curves at four box domains in (a) are shown in (c-f), with red symbols indicating two AOD thresholds and blue symbols indicating observed AOD from MODIS. Chinese regions with low aerosol-free NPP (<0.05 g C m^{-2} day^{-1}) are blanked in (a-b). Color scales for (a) and (b) are different.
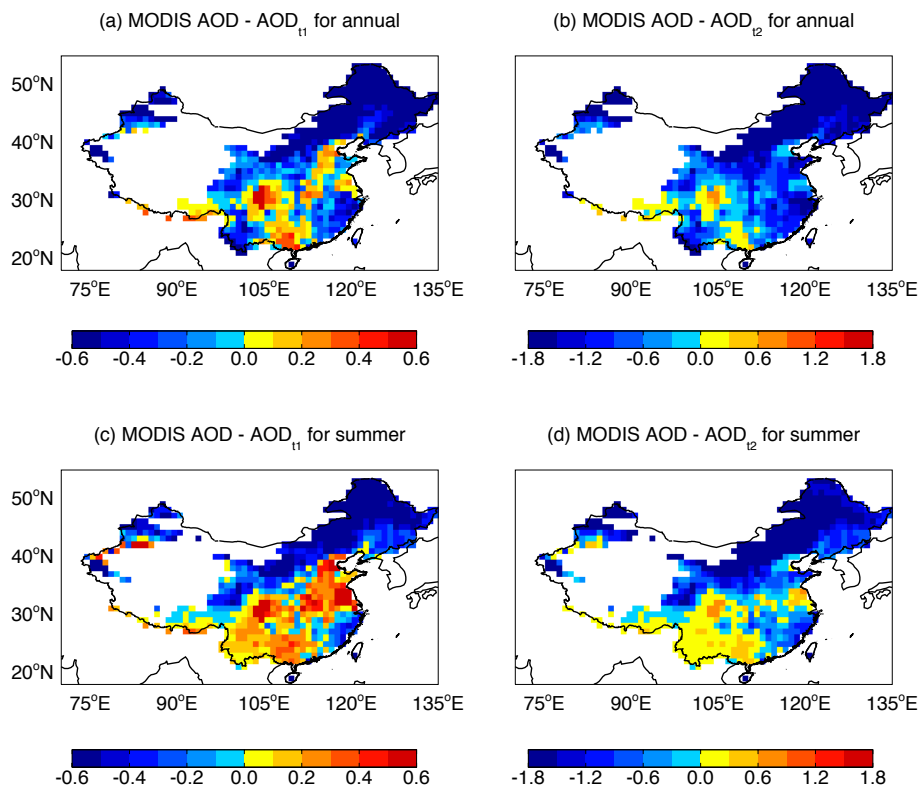
Atmospheric
Chemistry
and Physics
Discussions

Figure 7. Differences between MODIS AOD and two derived AOD thresholds. Left panel shows ΔAOD between MODIS and AOD_{t1} for the average of (a) whole year and (c) summer months. Right panel shows ΔAOD between MODIS and AOD_{t2} for the average of (b) whole year and (d) summer months. For the left panel, regions with positive values indicate that increase (decrease) of local AOD leads to reductions (enhancement) in NPP, while regions with negative values denote that decrease (increase) of local AOD results in reductions (enhancement) in NPP. For the right panel, regions with negative (positive) values indicate that current level of AOD always promotes (inhibits) NPP, compared with the aerosol-free conditions. The color scales among panels are different.
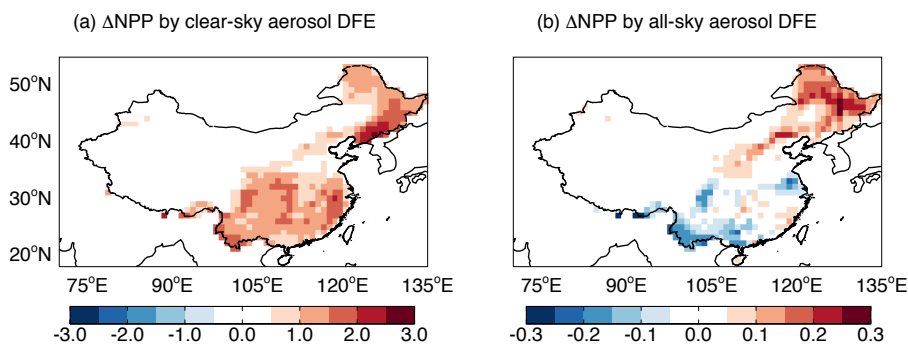
Atmospheric
Chemistry
and Physics
Discussions

Figure 8. Changes in summer NPP caused by aerosol DFE in China for (a) clear-sky (CLR010 – CLR000) and (b) all-sky (ALL010 – ALL000) conditions. The color scales between panels are different. Units: g C m^{-2} day^{-1}.